

Current-Dependent Morphologies of Insulating Electrodeposits in Li–O₂ Batteries Controlled by Coupled Ion-Electron Transfer Kinetics

Penghao Zhang, Shakul Pathak, Martin Z. Bazant,* and Peng Bai*

Cite This: <https://doi.org/10.1021/acsami.5c03369>

Read Online

ACCESS |



Metrics & More



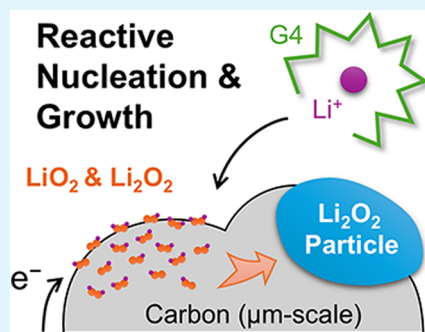
Article Recommendations



Supporting Information

ABSTRACT: Lithium–oxygen batteries (Li–O₂) present a compelling prospect for the next generation of batteries owing to their exceptionally high theoretical energy density. However, the performance of Li–O₂ batteries remains limited by the formation of insulating oxides covering the gas electrode, leading to low capacity or even unexpected sudden death. Existing mathematical models using Butler–Volmer kinetics exhibit uncertainties and inaccuracies in predicting the voltage responses and the morphological evolution of the insulating oxides. In this study, we incorporate coupled ion–electron transfer theory with a phase–field model to enable consistent predictions of the voltage curves, oxide morphologies, and roles of solvation energy. This study provides a valuable predictive tool for the predictive design of electrolytes and electrodes for batteries forming insulating products.

KEYWORDS: metal–air battery, phase formation, phase–field modeling, charge–transfer kinetics, solvation energy



1. INTRODUCTION

Among the available rechargeable batteries, lithium–oxygen (Li–O₂) batteries are distinguished by their remarkable specific energy densities, which can reach up to 5200 Wh/kg, much higher than the 200 Wh/kg offered by lithium-ion batteries. This makes Li–O₂ batteries promising candidates for electric vehicle propulsion and a wide range of other applications.¹ However, the practical deployment of Li–O₂ batteries faces formidable challenges.² One major issue is the uncertainty of discharge capacities due to the formation of lithium peroxide (Li₂O₂).^{3,4} This insulating discharge product accumulated on the gas electrode surface obstructs the transport of both oxygen and electrons, thereby limiting the discharge capacity. Recent studies also identified that Li₂O₂ exhibited a current-dependent morphology.⁵ At low current densities, Li₂O₂ tends to form large islands, leaving some active surface areas for the continued reactions. In contrast, at high current densities, Li₂O₂ forms as a thin film, blocking available reacting sites and resulting in premature, sudden death of the cell.⁶ To mitigate this issue, multimodal optimizations of electrode materials, electrolyte compositions, separator designs, and operation protocols become necessary. However, all these efforts converge on the key question of how to control the Li₂O₂ morphology on the porous gas electrode surfaces.⁷ Establishing a precise understanding of the current-dependent morphology of Li₂O₂ could be invaluable for guiding further optimizations of Li–O₂ batteries.

Mathematical modeling has proven to be a cost-effective and efficient tool for optimizing battery designs through a quantitative and predictive understanding of fundamental mechanisms.^{8–13} Horstmann et al. successfully predicted

current-dependent morphology by combining generalized Butler–Volmer (BV) kinetics¹⁴ with an epitaxial surface growth model.¹⁵ This model was the first to capture a current-dependent morphological transition from island to film growth, inspiring subsequent studies on the current-dependent formation process of Li₂O₂.^{16–19} This morphology selection in reaction-limited electrodeposition exemplifies the control of pattern formation by electro-autocatalysis,²⁰ analogous to the suppression of phase separation by electro-autoinhibitory ion intercalation in lithium iron phosphate (LFP)^{21–23} and the onset of fictitious phase separation in layered oxides by electro-autocatalytic ion deintercalation in layered nickel–manganese–cobalt (NMC) oxides.²⁴

Despite the success in capturing the general trend, various inconsistencies in the detailed features and dynamic behaviors necessitate further improvement of the model. A notable drawback of the BV kinetics lies in its phenomenological symmetry factor or charge transfer coefficient α , which is conventionally assigned a default value of 0.5 or fitted from a Tafel plot without satisfactory microscopic physical explanations.^{25–27} As exemplified in Figure 1, using the BV kinetics to fit either the linear part of the Tafel plot or the full data set yields a 3-fold difference in α values. When transport effects can be safely excluded, curved Tafel plots indicate a self-

Received: February 17, 2025

Revised: May 7, 2025

Accepted: May 26, 2025

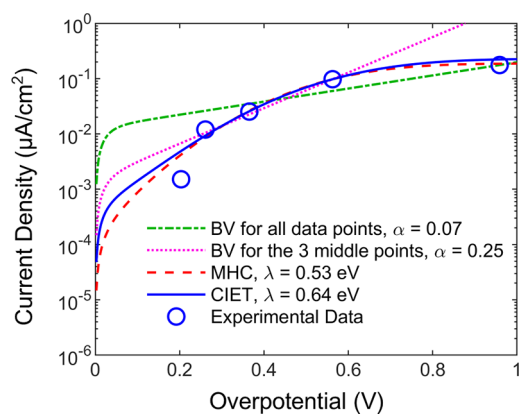


Figure 1. Tafel plot fitting for Li–O₂ batteries with different kinetic models. Data points were digitized from previous work⁵ with permission (Copyright 2025 Royal Society of Chemistry).

limiting reaction mechanism where electron transfer is the limiting step.²⁸ In such cases, the microscopic electron transfer (ET) theory, first proposed by Marcus and further developed by others,^{29,30} provides a physics-based framework to understand reaction kinetics via an outer-sphere electron transfer process. Marcus kinetics for heterogeneous reactions at the electrode surface, which takes into account the energetics of electrons in the electrode, was experimentally verified by Chidsey^{31,32} and popularized as the Marcus–Hush–Chidsey (MHC) formula. The MHC formula incorporates local effects from the electrode–electrolyte interfacial environment and ion (de)solvation into reaction kinetics via parameters such as the density of states of the electron donor (χ) and reorganization energy (λ).³² Using MHC kinetics to fit the same data set, as shown in Figure 1 demonstrates much better agreement. However, neither the phenomenological BV kinetics nor the microscopic MHC kinetics distinguishes between the roles of ion transfer and electron transfer, precluding a thorough mechanistic physical understanding.

Recently, Marcus theory and Butler–Volmer kinetics were unified and extended within a single, quantum mechanical framework of coupled ion–electron transfer (CIET) theory.^{33,34} CIET unifies two different dynamic regimes. In electron transfer-limited cases, it is electron-coupled ion transfer (ECIT), while in ion transfer-limited cases, it is ion-coupled electron transfer (ICET). More details on the derivation and discussions on the differences can be found elsewhere.³³ In the case of electrodeposition of insulating Li₂O₂ products, the reaction is more likely to be electron transfer-limited ECIT than ion transfer-limited ICET. Indeed, as seen in Figure 1, fitting the same Tafel data⁵ using CIET yields an agreement comparable to that of MHC and much better than Butler–

Volmer kinetics. It is worth noting that only the first four points were used in the fitting, and the theoretical prediction passes through the fifth point at the higher overpotential. The results suggest combining CIET with the phase-field model to revisit the electrochemical formation process of insulating products in batteries using Li–O₂ batteries as a model system. The linear stability analysis of Horstmann et al.¹⁵ has been generalized by Fraggadakis and Bazant for the Marcus kinetics of electron transfer at metallic and insulating electrode surfaces and shown the importance of quantum mechanics in controlling pattern formation on the electrode surface.⁵⁸ Here, we investigate the possible role of CIET kinetics in controlling the morphology of insulating electrodeposits under various dynamic conditions with experimental validations.

2. MATHEMATICAL MODELING

The formation of Li₂O₂ may follow different pathways.^{35,36} For the tetraglyme (G4) solvent we used in this study, the electrochemical reduction of O₂ proceeds via a two-step reaction on the surface of the carbon electrode,³⁵ as illustrated in Figure 2. The first step involves a one-electron transfer reaction, Li⁺ + O₂ + e[−] → LiO₂, to generate the intermediate LiO₂ (Figure 2a). The adsorbed LiO₂ will then be reduced by another one-electron transfer reaction with one additional Li⁺ to form the Li₂O₂ molecule: LiO₂ + Li⁺ + e[−] → Li₂O₂ (Figure 2b). In both steps, the charge transfer reaction involves electron transfer from the carbon substrate and ion transfer from the electrolyte, for which the phenomenological Butler–Volmer equation cannot establish explicit correlations between its fitting parameters and the physical properties of the respective processes. Physics-based microscopic kinetic theories, in contrast, allow the incorporation of the solvation energy to improve the mechanistic understanding.

At the molecular level, one may assume that the first one-electron transfer step to form the LiO₂ intermediate is rate-limiting, followed by the rapid formation of Li₂O₂ based on the standard redox potentials.³⁵ However, as first pointed out by Bai et al.,²¹ interfacial electrochemical reactions are influenced by (bulk) material thermodynamics when solid particles are involved or formed. The nucleation and growth of Li₂O₂ particles that occur concurrently with the formation of Li₂O₂ molecules must be considered simultaneously and modeled in a fully coupled manner. Therefore, in this study, we investigate the electrochemically reactive nucleation and growth of Li₂O₂ particles (Figure 2c), during which electrons are transferred from the carbon substrate while Li⁺ ions are transferred from the liquid electrolyte after desolvation from the G4 solvent molecules.

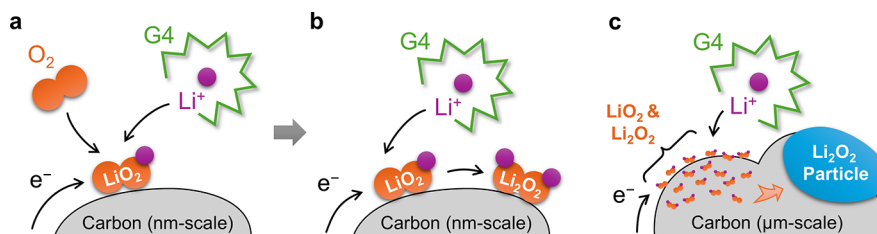


Figure 2. Li₂O₂ formation mechanism. (a) The first one-electron transfer reaction to form LiO₂ intermediate molecules, followed by (b) the second one-electron transfer reaction to form Li₂O₂ molecules. (c) Reactive nucleation and growth of Li₂O₂ particles.

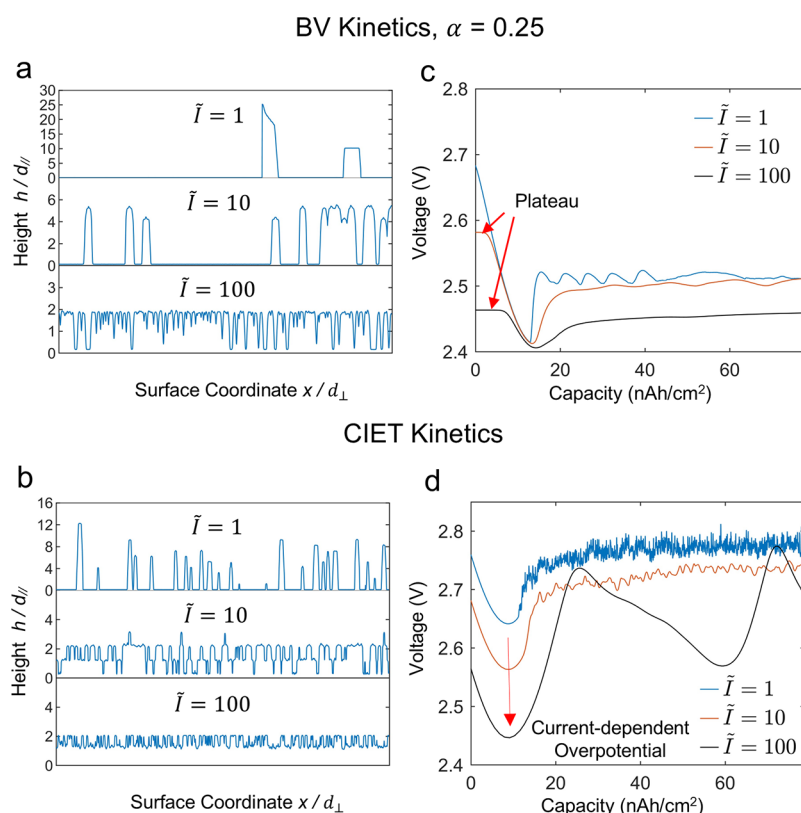


Figure 3. Simulated postdischarge morphologies (a,b) and the corresponding voltage profiles (c,d) from two kinetics models at various current densities. The initial voltage plateaus are indicated by red arrows in (c). The dip of voltage profiles corresponds to the nucleation barrier.

Following the method by Horstmann et al.,¹⁵ the dimensionless governing equation for reaction-limited electrodeposition/dissolution is

$$\frac{\partial \tilde{h}}{\partial \tilde{t}} = A \cdot \tilde{I}(\tilde{x}, \tilde{t}) \quad (1)$$

where $A = \sqrt{1 + \left(\frac{\partial h}{\partial x}\right)^2}$ is a geometrical factor converting substrate length to normal surface length and $\tilde{I}(\tilde{x}, \tilde{t})$ is a dimensionless current density derived from nonequilibrium electrochemical thermodynamics. Unless otherwise specified, all symbols with a tilde accent are dimensionless. The electrodeposition of Li_2O_2 is reflected through the height of the crystal $h(x)$, which varies as a function of projected surface coordinates. In this study, we incorporate and compare two distinct models of reaction kinetics, the BV kinetics used by Horstmann et al.¹⁵ and the electron transfer-limited CIET (i.e., ECIT) kinetics:³³

$$\text{BV kinetics: } I = I_0 [e^{-\alpha \tilde{\eta}} - e^{(1-\alpha)\tilde{\eta}}] \quad (2)$$

$$\text{CIET kinetics: } I = \frac{ek_0^*}{\gamma_{\ddagger}} e^{-\Delta \tilde{G}_{IT}} \left(\frac{c_O}{1 + e^{\tilde{\eta}_f}} - \frac{c_R}{1 + e^{-\tilde{\eta}_f}} \right) \text{erfc} \left(\frac{\tilde{\lambda} - \sqrt{1 + \tilde{\lambda} + \tilde{\eta}_f^2}}{2\sqrt{\tilde{\lambda}}} \right) \quad (3)$$

where $\tilde{\eta} = \Delta \tilde{\phi} - \Delta \tilde{\phi}_{eq}$ is the dimensionless surface overpotential; $\tilde{\lambda}$ is the Marcus reorganization energy for electron transfer (scaled to $k_B T$); $k_0^* = e\Delta_e/4\pi\hbar A_s$ is a quantum mechanical prefactor expressing the electronic coupling of the

donor and acceptor orbitals, where Δ_e is the chemisorption function; \hbar is the reduced Planck's constant; A_s is the area of a surface site for deposition; $\Delta \tilde{G}_{IT}$ is the constrained free energy of ion transfer from the electrolyte to the deposit without transferring the compensating electron; γ_{\ddagger} is the activity coefficient of the ion-transfer transition state; and α denotes the BV charge transfer coefficient, which is connected to the ion-transfer free energies for reduction and oxidation in the CIET theory.³³

The Nernst equilibrium voltage $\Delta \tilde{\phi}_{eq}$ and the exchange current density I_0 for the generalized BV kinetics¹⁴ are defined as follows:

$$\Delta \tilde{\phi}_{eq} = \ln \frac{a^+}{a} \quad \text{and} \quad I_0 = \frac{2ek_0 a^+}{\gamma_{\ddagger}} \quad (4)$$

where a denotes the activity of Li_2O_2 and a^+ represents the activity of Li^+ ions. Following the methodology outlined elsewhere,¹⁵ we assume $\alpha^+ = 1$ for the irreversible BV kinetics of reduction and $\gamma_{\ddagger} = 1$ to neglect the configurational entropy effects on the transition state, such as crowding of fixed active sites, since electrodeposits grow vertically unhindered. k_0 represents the rate constant determined through Tafel analysis, as documented in previous work.⁵ For the CIET theories, $\tilde{\eta}_f = \tilde{\eta} + \ln\left(\frac{c_O}{c_R}\right)$ is the formal overpotential.^{33,34} c_O and c_R are the dimensionless concentrations of oxidized and reduced species. In this case, $c_O = \alpha^+ = 1$ and $c_R = h$.

For a phase-separating system, the total free energy comprises two parts:

$$G = \int g_{\text{homo}} + \kappa \nabla^2 h dx \quad (5)$$

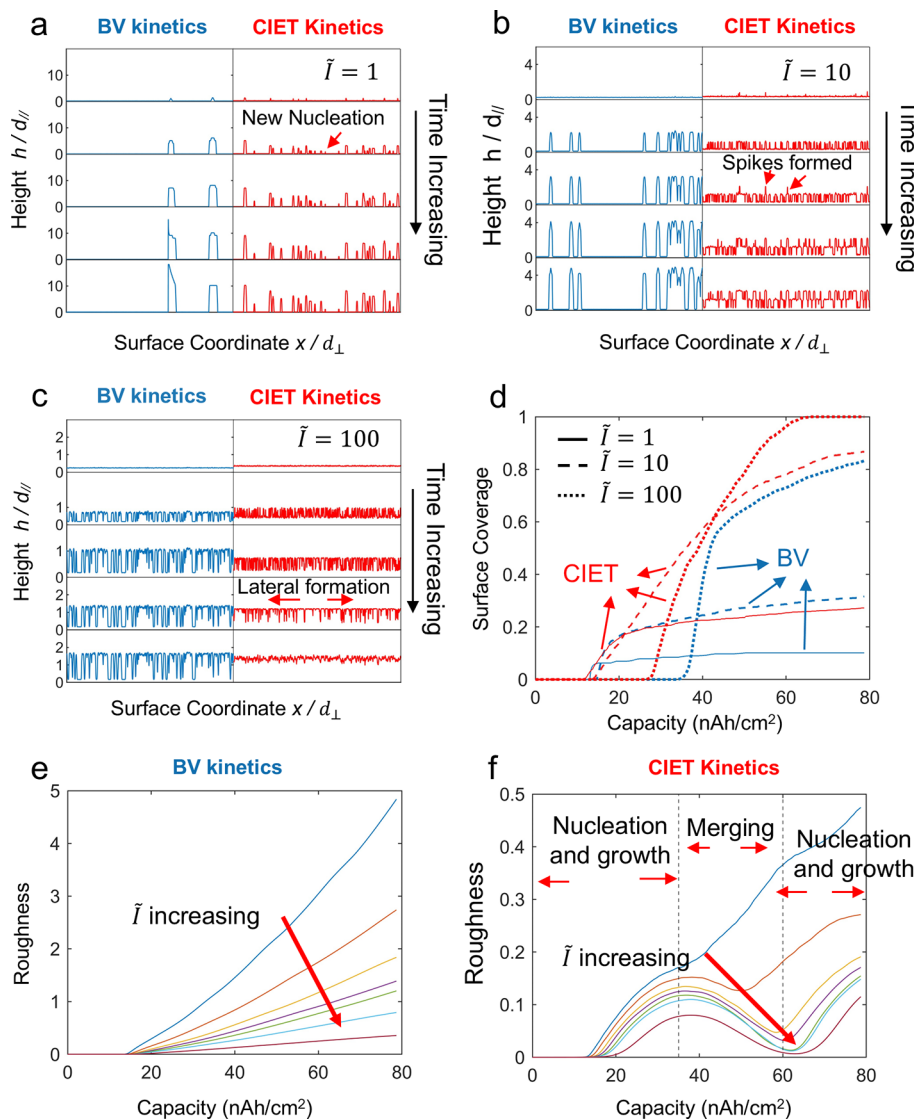


Figure 4. Analysis of the dynamic evolutions of the two models under low, intermediate, and high current densities. (a–c) Morphology evolutions, (d) surface coverage, and (e,f) surface roughness predicted by the two models under low, intermediate, and high current densities.

where g_{hom} is the homogeneous free energy density and κ is the Cahn–Hilliard gradient coefficient.³⁷ The chemical potential is defined as the variational derivative of the free energy:

$$\mu = \frac{\delta G}{\delta c} = d_{\parallel} d_{\perp} \frac{\delta G}{\delta h} = \mu_{\text{hom}} - \kappa \frac{\frac{\partial^2 h}{\partial x^2}}{\left[1 + \left(\frac{\partial h}{\partial x}\right)^2\right]^{3/2}}$$

$$= k_{\text{B}} T \ln a \quad (6)$$

where \tilde{h} is the dimensionless height of a Li_2O_2 crystal as a function of the projected surface coordinate \tilde{x} . We adopt the homogeneous free energy proposed by Horstmann et al.¹⁵

$$g_{\text{hom}} = \frac{2e}{d_{\perp} \pi} \left[E_1 \sin^2(\pi \tilde{h}) + \frac{1}{2} [A(\sigma_{\perp}^{1D} + \sigma_{\parallel}^{1D}) + \sigma_{\perp}^{1D} - \sigma_{\parallel}^{1D}] - E_2 e^{-\beta \tilde{h}^2 / 2} \right] \quad (7)$$

Solving eqs 1–7 allows a quantitative comparison between the BV kinetics and the CIET kinetics. All simulations were performed under the constant total current condition:

$$\tilde{I} = \frac{1}{L} \int_0^L \tilde{I} dx \quad (8)$$

where L is the length of the simulated surface.

Numerical integration with periodic boundary conditions was performed in MATLAB using implicit DAE-solver ode15s. The time step was automatically determined by the ode15s solver using its built-in adaptatively optimizing algorithm. The finite difference discretization method was applied for a 500 nm spatial domain. The physical meanings and the values of parameters d_{\perp} , d_{\parallel} , k_0 , κ , σ_{\perp}^{1D} , σ_{\parallel}^{1D} , E_1 , E_2 , and β are summarized in the Supporting Information (Sections 1.1–1.3). The nondimensionalization of all physical properties is also included in the Supporting Information (Table S1).

3. RESULTS

3.1. Simulations of Nucleation and Growth of Electrodeposits.

With these two different electrochemical

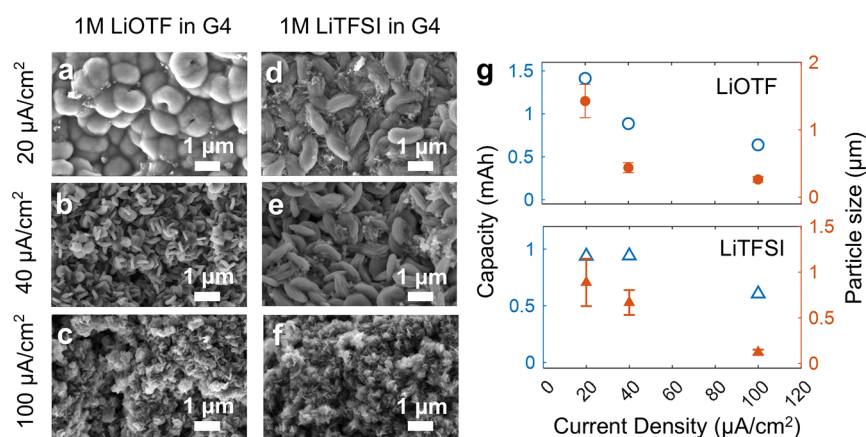


Figure 5. Postdischarge SEM images of cathodes using (a–c) LiOTF in G4 and (d–f) LiTFSI in G4. (g) Current-dependent postdischarge particle sizes for the two electrolytes. Cells were discharged from left to right at (1) 20 $\mu\text{A}/\text{cm}^2$, (2) 40 $\mu\text{A}/\text{cm}^2$, and (3) 100 $\mu\text{A}/\text{cm}^2$.

phase-field models, i.e., either with the BV kinetics or the CIET kinetics, we simulated the discharging process at various current densities and compared the end-of-discharge (~ 80 nAh/cm²) morphology profiles and the corresponding voltage profiles, as shown in Figure 3. Regarding the morphology profiles, both models predict a few tall and wide isolated growths at a low current density, but many shorter and narrower growths at higher current densities. At extremely high current densities, the entire simulation domain becomes fully covered by the growth spikes (nucleation centers or nuclei), which is interpreted as film growth as these nuclei will impinge very quickly and cover the entire substrate. Notably, at the same current densities, the number of growth spikes predicted by the CIET kinetics always surpasses that predicted by the BV kinetics. This is due to a key difference between BV and CIET, where BV always overpredicts the current density due to the lack of physical limitation. In other words, to yield the same current density, CIET requires a higher overpotential than BV does. Consequently, the higher overpotential in CIET activates more growth spikes (nucleation events).

The simulated voltage profiles also show significant differences. Both kinetics show voltage fluctuations at low current densities, which result from stochastic nucleation during discharging. The fluctuations appear more frequently with CIET kinetics than with BV kinetics.¹⁵ For the BV kinetics, as Horstmann et al. discovered, an initial voltage plateau (not observed in experiments though^{5,38}) always emerges and becomes more prominent as the current density increases (Figure 3c). However, the voltage minima, representing the nucleation overpotentials, show a negligible dependence on the applied current densities. In contrast, voltage profiles obtained from the CIET kinetics do not exhibit the initial voltage plateau and instead show a downward trajectory as the current density increases, which is consistent with experimental observations. This decreasing trend remains uniform across all of the current density values. The minimum voltage in the discharge curve shows a strong dependence on the applied current densities, consistent with the experiments. At high current densities, our model predicts a repeating pattern in the voltage curve, which is due to the uniform growth of full monolayers, reflecting the homogeneous free energy of the phase-field model.¹⁵ These comparisons clearly indicate that the CIET kinetics provides more physically realistic predictions than the BV kinetics.

Figure 4 summarizes further comparisons of the dynamic evolutions at every 13 nAh/cm² (corresponding to a 0.25 dimensionless capacity) predicted by the two models. Interestingly, once nucleation occurs, BV kinetics does not allow any new nucleation events regardless of the applied current densities. In contrast, CIET kinetics triggers new nucleation events throughout the entire discharging process. More importantly, negligible lateral growth is observed in BV kinetics, whereas lateral growths and the merging of the growths are common in the CIET kinetics. This behavior is revealed in the surface coverage over the discharge capacity curve in Figure 4d.

At low current densities (solid lines), both models predict similar surface coverage evolution over time. Initially, the coverage remained close to zero until the deposition process reached a critical point (the spinodal point, defined as the point when the voltage reaches its minimum). After this point, BV kinetics predict a sharp increase in coverage, followed by a limited but nearly constant coverage, indicating the formation of isolated growth that mainly grows taller. This behavior is observed at all current densities. In contrast, the CIET kinetics predicts a more gradual increase and more complete final coverage at all current densities, as shown by the red lines (solid, dash, and dot) in Figure 4d.

In addition to the coverage analysis, we propose a more quantitative method of analyzing the merging of isolated growths using the surface roughness. Roughness is defined as the height variance and plotted against the discharge-specific capacities, as shown in Figure 4e,f. For BV kinetics, the roughness increases monotonically, indicating little to no merging behavior. As the current density increases, the overall roughness decreases but the monotonic trend remains. Surprisingly, the CIET kinetics predicts not only a decrease in roughness due to the merging of growths but also a recurrence of the roughness due to the new nucleation events, resulting in a periodic pattern. At higher current densities, this periodic pattern becomes more prominent. This non-monotonic dynamic process, while appearing natural, has not been captured by any previous physics-based mathematical models and cannot be captured by BV kinetics. This growth–merging–nucleation mechanism can also be seen in the experiments conducted by Lau and Archer.³⁹ The agreement between theoretical predictions and independent experimental discoveries encouraged further systematic experimental validations.

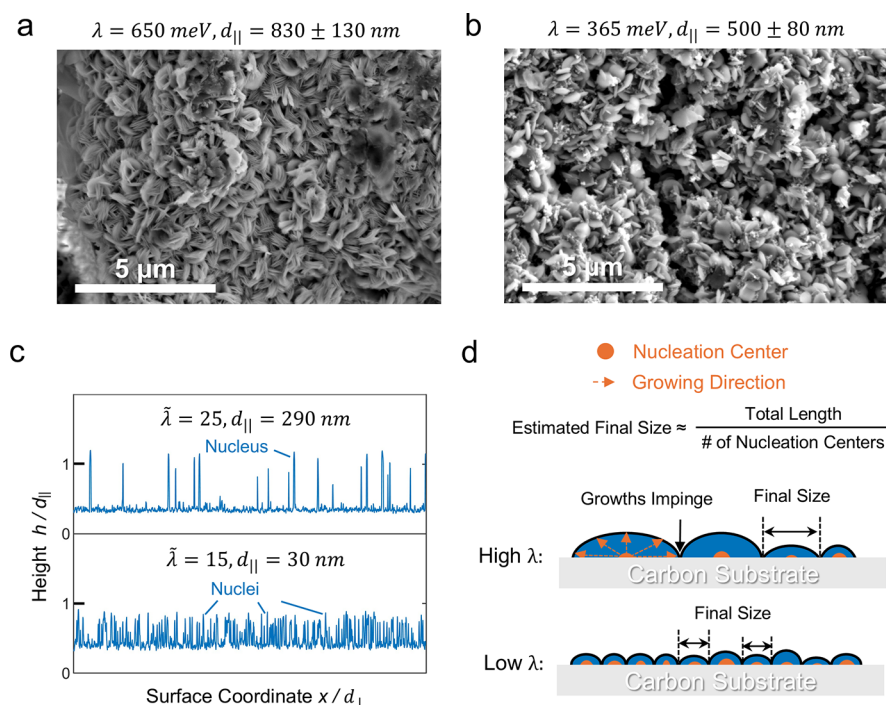


Figure 6. Postdischarge SEM images of oxides on the cathodes using (a) 0.1 M LiPF₆ in DMSO and (b) 0.1 M LiPF₆ in G4. Cells were discharged at 100 μA/cm². (c) Simulated morphology profiles using CIET kinetics. (d) Schematic diagram of particle size estimation. All three simulations were performed under the same $\tilde{I} = 10$. For $\tilde{\lambda} = 25$, the surface coverage is 43%. For $\tilde{\lambda} = 15$, the surface coverage is 93%. Each spike represents an individual nucleation center, and the estimated final particle size is the total length of the substrate divided by the number of spikes, as schematically explained in (d).

3.2. Experimental Validations. To validate the theoretical predictions, we followed the method by Lau and Archer³⁹ to construct an experimental setup for testing Li–O₂ coin cells. A schematic diagram of this apparatus, along with details of the experimental approach and testing methodology, can be found in the (Supporting Information, Figure S1). CR2032 coin cells were assembled using lithium foil (MTI) as the anode. The cathode was prepared via a slurry casting method, composed of conductive acetylene carbon black (MTI) with a 10% poly(vinylidene fluoride) (PVDF) binder. More details on cathode preparation can be found in the Supporting Information (Section 2.1). The coin cells were discharged at various constant current densities ranging from 20 to 200 μA/cm² (normalized to the geometric cathode area) inside a hermetically sealed oxygen chamber.

Figure 5 presents the SEM images of the end-of-discharge products on carbon electrodes in two different electrolytes at various current densities along with the corresponding current-dependent particle sizes and capacities. The Gaussian distribution of all SEM analyses and the method of determining the particle size experimentally are included in the Supporting Information (Sections 2.7–2.8).

Increasing current densities, driven by higher overpotentials, leads to a decrease in particle sizes but an increase in particle numbers, as observed in Figure 5a–f. The trend of particle size reduction shows a strong correlation with the attainable discharge capacity in both electrolytes (Figure 5g). Since the particle growth is the direct result of electrochemical processes, we hypothesize that the electrochemical overpotential, equivalently the effective charge transfer energy barrier, is the dominating factor. The CIET kinetics provides the physical connection between the overpotential and the energy barrier via the physical parameter reorganization energy (λ), which

reflects the energy required to reorganize the local solvation environment to enable the charge transfer and new phase formation. If the local solvation environments of the two electrolytes are very similar, then Li₂O₂ should form particles with similar sizes under the same current density. Indeed, recent molecular dynamics (MD) simulations and density functional theory (DFT) calculations conducted by Saito et al. revealed that the solvation energies of the two electrolytes we used (Figure 4) are very similar, –6.10 eV for LiOTF in G4 versus –5.97 eV (*cis*)/–6.04 eV (*trans*) for LiTFSI in G4.⁴⁰

To further verify our hypothesis, we conducted additional tests using 0.1 M LiPF₆ in DMSO and 0.1 M LiPF₆ in G4 as the electrolytes. Based on the rotating ring-disk electrode (RRDE) experiments by Sankarasubramanian et al.,⁴¹ the reorganization energy of DMSO ($\lambda = 650$ meV $\rightarrow \tilde{\lambda} = 25$) is greater than that of G4 ($\lambda = 365$ meV $\rightarrow \tilde{\lambda} = 15$). As can be seen in Figure 6a,b, the particle sizes are noticeably different. Simulations using the CIET kinetics with consistent reorganization energies also show different numbers of nucleation centers, which can be used to infer the final size of the particles by dividing the total length of the simulated substrate by the number of nuclei, as schematically explained in Figure 6d.

The substrate length of the simulation is 500 nm. We stopped the simulation as soon as any particles reached the height of the first monolayer ($\tilde{h} = 1$). Each spike represents a nucleation center. As demonstrated in Figure 6c, under the same current density, a greater $\tilde{\lambda}$ leads to a lower number of spikes, indicating a larger eventual particle size. The schematic diagram of theoretical particle size estimation is shown in Figure 6d. Particle growths stop when they impinge each other. Therefore, the average final particle size can be estimated as the total length of the substrate divided by the number of nucleation centers.

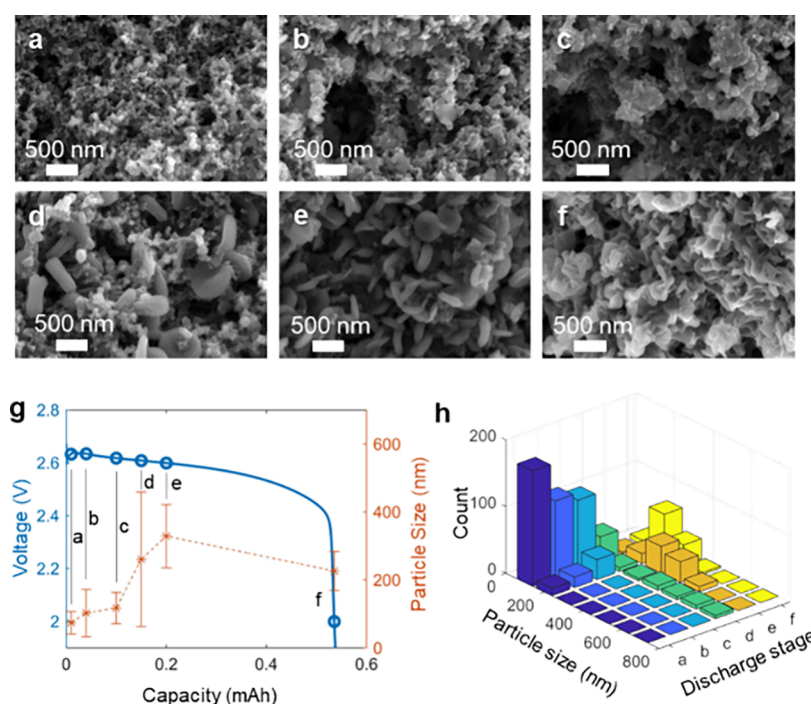


Figure 7. Post-mortem analysis at different capacities. SEM images of the cathodes discharged at $100 \mu\text{A}/\text{cm}^2$ in 1 M LiOTf in G4 and stopped at (a) 0.01 mAh, (b) 0.04 mAh, (c) 0.1 mAh, (d) 0.15 mAh, (e) 0.2 mAh, and (f) the end of discharging at 2 V. (g) Corresponding discharge voltage curve and average particle size. (h) Corresponding particle size distributions.

To verify the theoretical prediction of the merging of growths and the new nucleation, we conducted ex situ post-mortem experiments on discharge products obtained at different stages of the discharge. The results are presented in Figure 7. Similar to the work by Lau and Archer,³⁹ small round particles, approximately 100 nm in size, were observed at the beginning of the discharge (0.01 mAh, Figure 7a). Here, only the bright (less conductive) particles were counted, as the darker particles are the carbon particles from the gas electrode. From Figure 7a–c, more particles formed and eventually covered all nanosized carbon particles. These particles then began to form larger disc-shaped particles, as seen in Figure 7d, resulting in a bimodal particle size distribution. By stage (e), almost all of the small round particles merged to form uniformly sized, larger disc-shaped particles (~ 300 nm, Figure 7e), confirming the merging/coarsening process. At the end of discharging (Figure 7f), smaller particles (~ 200 nm) reappeared, which can only be attributed to the formation of new particles on top of the larger particles seen in stage (e). While the merging of growths is not surprising, the phase-field model with the BV kinetics cannot predict this and instead suggests only the growth in height (Figure 4). Our new phase-field model with the CIET kinetics predicts not only the merging of isolated growing particles but also the new nucleation events on top of the merged layers, as reflected in Figure 4f (simulations) and Figure 7e,f (experiments).

4. DISCUSSION

The agreement between our experimental observations and the theoretical predictions across all three aspects, current dependence, morphological evolution, and the role of solvation energies, demonstrates the predictive capability and accuracy of CIET kinetics. Coupling with the phase-field model incorporates the bulk material thermodynamics from the

solid particles, while the microscopic formulation of reaction kinetics establishes the direct connection with the molecular level electrolyte properties. The CIET phase-field model that we developed here provides a tool to analyze complex interfacial dynamics. In the case of the electrodeposition of insulating particles, electron transfer is rate-limiting for the concurrent reduction reaction and phase formation. The CIET theory predicts the MHC kinetics but with modified prefactors for the reduction and oxidation rates accounting for ion transfer.^{33,34} In this dynamic regime, the CIET is defined as electron-coupled ion transfer theory (ECIT), which was first proposed for lithium intercalation in the insulating electrode LFP, limited by electron transfer from the carbon coating to the nearest iron redox site.⁴² The predicted concentration dependence has been verified by learning from a large data set of X-ray images of LFP nanoparticles.²³ Experimental evidence for this regime of CIET has also been obtained for a variety of popular Li-ion battery electrode materials,⁴³ and the theory has been used in the *ab initio* quantum predictions of Faradaic reaction rates for lithium intercalation in lithium cobalt oxide (Li_xCoO_2) from different electrolytes.⁴⁴ The theory has also been applied successfully to lithium intercalation and degradation of NMC cathodes^{45–47} and graphite anodes^{48–50} in Li-ion batteries, SEI growth^{51–53} and proton intercalation⁵⁴ in solid-oxide fuel cells, and carbon dioxide reduction by electrocatalysis.^{55,56} If ion transfer is rate-limiting, then the CIET theory provides the first fundamental, quantum mechanical derivation of the Butler–Volmer equation, where the exchange current and symmetry factor are related to the ion transfer, reorganization energies, electronic coupling, and various thermodynamic factors.³³ This reaction model (“ion-coupled electron transfer”, ICET), has been applied to solid electrolyte interphase (SEI) growth⁵⁷ and effectively underpins all previous uses of Butler–Volmer kinetics, including the original model of Li_2O_2 growth by Horstmann et al.¹⁵ The

theory also predicts the breakdown of the Butler–Volmer kinetics at high overpotentials, leading to a quantum mechanical limiting current.³³

5. CONCLUSIONS

In this study, we conducted a comparative analysis of the classic BV kinetics and the CIET kinetics in modeling the current-dependent formation processes of insulating oxides in Li–O₂ batteries and validated the predictions in experiments. We identified significant differences in theoretical predictions regarding discharge profiles, postdischarge morphologies, dynamic evolution behaviors, and the roles of solvation energies in different electrolytes, where the CIET kinetics agree with experimental results much better than those from the BV kinetics. More importantly, CIET kinetics, due to a more realistic current–overpotential relationship, allows the merging and coarsening of isolated growths that may occur naturally in all formation processes. In contrast, BV kinetics preferentially focuses the reaction flux only on the existing nucleation centers, with negligible lateral growths. CIET kinetics, through the physics-based reorganization energy, enables the incorporation of solvation energy from liquid electrolytes accounting for the chemistry-specific properties of the discharge product. In contrast, the phenomenological BV kinetics cannot explicitly reflect the electrolyte properties. All these predictions find good agreement with experimental results using different electrolytes. Our CIET phase-field model offers a platform for studying other formation processes, including the SEI layer formed on alkali metal anodes and the insulating Li₂S formed in Li–S batteries.⁵⁹ The fundamental understanding of the experimental results using our model offers valuable guidance for the synergistic design of electrolyte formulations, electrode microstructures and surfaces, and optimal operation protocols.

■ ASSOCIATED CONTENT

SI Supporting Information

The Supporting Information is available free of charge at <https://pubs.acs.org/doi/10.1021/acsami.5c03369>.

Derivation of the CIET-based model of the Li₂O₂ formation process, nondimensionalization summary, details of the experimental approach and schematic diagram of apparatus, particle size measurements, and Gaussian analysis of SEM images (PDF)

■ AUTHOR INFORMATION

Corresponding Authors

Martin Z. Bazant – Department of Chemical Engineering and Department of Mathematics, Massachusetts Institute of Technology, Cambridge, Massachusetts 02139, United States; orcid.org/0000-0002-8200-4501; Email: bazant@mit.edu

Peng Bai – Department of Energy, Environmental and Chemical Engineering and Institute of Materials Science and Engineering, Washington University in St. Louis, St. Louis, Missouri 63130, United States; orcid.org/0000-0002-2419-3498; Email: pbai@wustl.edu

Authors

Penghao Zhang – Department of Energy, Environmental and Chemical Engineering, Washington University in St. Louis, St. Louis, Missouri 63130, United States

Shakul Pathak – Department of Chemical Engineering, Massachusetts Institute of Technology, Cambridge, Massachusetts 02139, United States; orcid.org/0009-0006-3244-1670

Complete contact information is available at: <https://pubs.acs.org/10.1021/acsami.5c03369>

Notes

The authors declare no competing financial interest.

■ ACKNOWLEDGMENTS

This work was partially supported by a National Science Foundation grant (Award No. 2044932) and an ARPA-E PROPEL-1K grant (Award No. DE-AR0001884). The materials characterization experiments were partially supported by IMSE (Institute of Materials Science and Engineering). The authors thank Dr. Vijay Ramani and Dr. Xianglin Li for helpful discussions.

■ REFERENCES

- (1) Kwak, W.-J.; Rosy, S.; Sharon, D.; Xia, C.; Kim, H.; Johnson, L.; Bruce, P.; Nazar, L.; Sun, Y.-K.; Frimer, A.; Noked, M.; Freunberger, S.; Aurbach, D. Lithium–Oxygen Batteries and Related Systems: Potential, Status, and Future. *Chem. Rev.* **2020**, *120*, 6626–6683.
- (2) McCloskey, B. D.; Valery, A.; Luntz, A. C.; Gowda, S. R.; Wallraff, G. M.; Garcia, J. M.; Mori, T.; Krupp, L. E. Combining Accurate O₂ and Li₂O₂ Assays to Separate Discharge and Charge Stability Limitations in Nonaqueous Li–O₂ Batteries. *J. Phys. Chem. Lett.* **2013**, *4*, 2989–2993.
- (3) Read, J. Characterization of the Lithium/Oxygen Organic Electrolyte Battery. *J. Electrochem. Soc.* **2002**, *149*, A1190–A1195.
- (4) Albertus, P.; Girishkumar, G.; McCloskey, B.; Sanchez-Carrera, R. S.; Kozinsky, B.; Christensen, J.; Luntz, A. C. Identifying Capacity Limitations in the Li/Oxygen Battery Using Experiments and Modeling. *J. Electrochem. Soc.* **2011**, *158*, A343.
- (5) Gallant, B. M.; Kwabi, D. G.; Mitchell, R. R.; Zhou, J.; Thompson, C. V.; Shao-Horn, Y. Influence of Li₂O₂ Morphology on Oxygen Reduction and Evolution Kinetics in Li–O₂ Batteries. *Energy Environ. Sci.* **2013**, *6*, 2518.
- (6) Adams, B. D.; Radtke, C.; Black, R.; Trudeau, M. L.; Zaghbib, K.; Nazar, L. F. Current Density Dependence of Peroxide Formation in the Li–O₂ Battery and Its Effect on Charge. *Energy Environ. Sci.* **2013**, *6*, 1772.
- (7) Yang, X.; He, P.; Xia, Y. Preparation of Mesocellular Carbon Foam and Its Application for Lithium/Oxygen Battery. *Electrochem. Commun.* **2009**, *11* (5), 1127–1130.
- (8) Xiao, J.; Mei, D.; Li, X.; Xu, W.; Wang, D.; Graff, G. L.; Bennett, W. D.; Nie, Z.; Saraf, L. V.; Aksay, I. A.; Liu, J.; Zhang, J.-G. Hierarchically Porous Graphene as a Lithium–Air Battery Electrode. *Nano Lett.* **2011**, *11*, 5071–5078.
- (9) Read, J.; Mutolo, K.; Ervin, M.; Behl, W.; Wolfenstine, J.; Driedger, A.; Foster, D. Oxygen Transport Properties of Organic Electrolytes and Performance of Lithium/Oxygen Battery. *J. Electrochem. Soc.* **2003**, *150*, A1351.
- (10) Sandhu, S.; Fellner, J.; Brutchen, G. Diffusion-limited model for a lithium/air battery with an organic electrolyte. *J. Power Sources* **2007**, *164*, 365–371.
- (11) Mehta, M.; Bevara, V.; Andrei, P. Limitations and Potential of Li–Air Batteries: A Simulation Prediction. *Proc. IEEE* **2012**, *241*, 241–244.
- (12) Sahapatombut, U.; Cheng, H.; Scott, K. Modelling of electrolyte degradation and cycling behaviour in a lithium–air battery. *J. Power Sources* **2013**, *227*, 243–253.
- (13) Viswanathan, V.; Speidel, A.; Scheffler, R.; Gowda, S.; Luntz, A. C. DFT+U Study of Polaronic Conduction in Li₂O₂ and Li₂CO₃: Implications for Li–Air Batteries. *J. Phys. Chem. Lett.* **2013**, *4*, 556.

- (14) Bazant, M. Z. Theory of Chemical Kinetics and Charge Transfer Based on Nonequilibrium Thermodynamics. *Acc. Chem. Res.* **2013**, *46*, 1144–1160.
- (15) Horstmann, B.; Gallant, B.; Mitchell, R.; Bessler, W. G.; Shao-Horn, Y.; Bazant, M. Z. Rate-Dependent Morphology of Li₂O₂ Growth in Li–O₂ Batteries. *J. Phys. Chem. Lett.* **2013**, *4*, 4217–4232.
- (16) Knudsen, K. B.; Arrechea, P. L.; Viggiano, R. P.; Dornbusch, D. A.; Mullinax, J. W.; Bauschlicher, C. W.; Haskins, J. B.; Nguyen, B.; Lawson, J. W.; McCloskey, B. D. Amide- and Urea-Based Solvents for Li–O₂ Batteries. Part I: Experimental Evaluation. *J. Phys. Chem. C* **2023**, *127*, 7037–7042.
- (17) Zhang, P.; Han, B.; Yang, X.; Zou, Y.; Lu, X.; Liu, X.; Zhu, Y.; Wu, D.; Shen, S.; Li, L.; Zhao, Y.; Francisco, J. S.; Gu, M. Revealing the Intrinsic Atomic Structure and Chemistry of Amorphous LiO₂-Containing Products in Li–O₂ Batteries Using Cryogenic Electron Microscopy. *J. Am. Chem. Soc.* **2022**, *144*, 2129–2136.
- (18) Yi, X.; Liu, X.; Dou, R.; Wen, Z.; Zhou, W. Understanding the Catalytic Activity of the Preferred Nitrogen Configuration on the Carbon Nanotube Surface and Its Implications for Li–O₂ Batteries. *J. Phys. Chem. C* **2021**, *125*, 22570–22580.
- (19) Batcho, T. P.; Leverick, G.; Shao-Horn, Y.; Thompson, C. V. Modeling the Effect of Lithium Superoxide Solvation and Surface Reduction Kinetics on Discharge Capacity in Lithium–Oxygen Batteries. *J. Phys. Chem. C* **2019**, *123*, 14272–14282.
- (20) Bazant, M. Z. Thermodynamic Stability of Driven Open Systems and Control of Phase Separation by Electro-autocatalysis. *Faraday Discuss.* **2017**, *199*, 423–463.
- (21) Bai, P.; Cogswell, D. A.; Bazant, M. Z. Suppression of Phase Separation in LiFePO₄ Nanoparticles During Battery Discharge. *Nano Lett.* **2011**, *11* (11), 4890–4896.
- (22) Cogswell, D. A.; Bazant, M. Z. Coherency Strain and the Kinetics of Phase Separation in LiFePO₄ Nanoparticles. *ACS Nano* **2012**, *6* (3), 2215–2225.
- (23) Zhao, H.; et al. Learning Heterogeneous Reaction Kinetics from X-ray Videos Pixel by Pixel. *Nature* **2023**, *621* (7978), 289–294.
- (24) Park, J.; et al. Fictitious Phase Separation in Li Layered Oxides Driven by Electro-autocatalysis. *Nat. Mater.* **2021**, *20* (7), 991–999.
- (25) Wang, F.; Li, X. Pore Scale Simulations of Porous Electrodes of Li–O₂ Batteries at Different Saturation Levels. *ACS Appl. Mater. Interfaces* **2018**, *10* (31), 26222–26232.
- (26) Yoo, K.; Banerjee, S.; Dutta, P. Modeling of volume change phenomena in a Li-air battery. *J. Power Sources* **2014**, *258*, 340–350.
- (27) Mehta, M.; Bevara, V.; Andrei, P. Maximum theoretical power density of lithium–air batteries with mixed electrolyte. *J. Power Sources* **2015**, *286*, 299–308.
- (28) Fletcher, S.; Varley, T. Beyond the Butler-Volmer Equation: Curved Tafel Slopes from Steady-State Current-Voltage Curves. *Phys. Chem. Chem. Phys.* **2011**, *13*, 5359–5364.
- (29) Marcus, R. A. Chemical and Electrochemical Electron-Transfer Theory. *Annu. Rev. Phys. Chem.* **1964**, *15*, 155–196.
- (30) Marcus, R. A. Electron Transfer Reactions in Chemistry: Theory and Experiment (Nobel Lecture). *Rev. Mod. Phys.* **1993**, *65*, 599–610.
- (31) Hush, N. S. Adiabatic Theory of Outer Sphere Electron-Transfer Reactions in Solution. *Trans. Faraday Soc.* **1961**, *57*, 557–580.
- (32) Chidsey, C. E. D. Free Energy and Temperature Dependence of Electron Transfer at the Metal-Electrolyte Interface. *Science* **1991**, *251*, 919–922.
- (33) Bazant, M. Z. Unified Quantum Theory of Electrochemical Kinetics by Coupled Ion-Electron Transfer. *Faraday Discuss.* **2023**, *246*, 60–124.
- (34) Fraggedakis, D.; McEldrew, M.; Smith, R. B.; Krishnan, Y.; Zhang, Y.; Bai, P.; Chueh, W. C.; Shao-Horn, Y.; Bazant, M. Z. Theory of Coupled Ion-Electron Transfer Kinetics. *J. Chem. Phys.* **2021**, *152*, No. 184703.
- (35) Aurbach, D.; McCloskey, B. D.; Nazar, L. F.; Bruce, P. G. Advances in Understanding Mechanisms Underpinning Lithium–Air Batteries. *Nat. Energy* **2016**, *1*, 16128.
- (36) Bruce, P. G.; Freunberger, S. A.; Hardwick, L. J.; Tarascon, J.-M. Li–O₂ and Li–S Batteries with High Energy Storage. *Nat. Mater.* **2012**, *11*, 19–29.
- (37) Cahn, J. W.; Hilliard, J. E. Free Energy of a Nonuniform System. I. Interfacial Free Energy. *J. Chem. Phys.* **1958**, *28* (2), 258–267.
- (38) Laoire, C.; Mukerjee, S.; Abraham, K. M.; Plichta, E. J.; Hendrickson, M. A. Influence of Nonaqueous Solvents on the Electrochemistry of Oxygen in the Rechargeable Lithium–Air Battery. *J. Phys. Chem. C* **2009**, *113*, 20127–20134.
- (39) Lau, S.; Archer, L. A. Nucleation and Growth of Lithium Peroxide in the Li–O₂ Battery. *Nano Lett.* **2015**, *15*, 5995–6114.
- (40) Saito, M.; Yamada, S.; Ishikawa, T.; Otsuka, H.; Ito, K.; Kubo, Y. Development of Electrolyte Materials for Lithium–Oxygen Batteries. *RSC Adv.* **2017**, *7*, 49031–49040.
- (41) Sankarasubramanian, S.; Seo, J.; Mizuno, F.; Singh, N.; Prakash, J. Elucidating the Oxygen Reduction Reaction Kinetics and the Origins of the Anomalous Tafel Behavior at the Lithium–Oxygen Cell Cathode. *J. Phys. Chem. C* **2017**, *121* (1), 4789.
- (42) Bai, P.; Bazant, M. Z. Charge Transfer Kinetics at the Solid–Solid Interface in Porous Electrodes. *Nat. Commun.* **2014**, *5* (1), 3585.
- (43) Zhang, Y.; Fraggedakis, D.; Gao, T.; Pathak, S.; Zhuang, D.; Grosu, C.; et al. Lithium-Ion Intercalation by Coupled Ion-Electron Transfer. *ChemRxiv* **2024**.
- (44) Halldin Stenlid, J.; et al. Computational Insights into Electrolyte-Dependent Li-Ion Charge-Transfer Kinetics at the Li_xCoO₂ Interface. *ACS Energy Lett.* **2024**, *9* (7), 3608–3617.
- (45) Zhuang, D.; Bazant, M. Z. Population Effects Driving Active Material Degradation in Intercalation Electrodes. *Phys. Rev. E* **2023**, *107*, No. 044603.
- (46) Zhuang, D.; Bazant, M. Z. Theory of Layered-Oxide Cathode Degradation in Li-Ion Batteries by Oxidation-Induced Cation Disorder. *J. Electrochem. Soc.* **2022**, *169*, No. 100536.
- (47) Zhuang, D.; et al. Physics-Informed Design of Hybrid Pulse Power Characterization Tests for Rechargeable Batteries. *J. Electrochem. Soc.* **2024**, *171* (5), No. 050510.
- (48) Gao, T.; et al. Interplay of Lithium Intercalation and Plating on a Single Graphite Particle. *Joule* **2021**, *5* (2), 393–414.
- (49) Ahn, S.; et al. Chemical Origins of a Fast-Charge Performance in Disordered Carbon Anodes. *ACS Appl. Energy Mater.* **2023**, *6* (16), 8455–8465.
- (50) Lian, H.; Bazant, M. Z. Modeling Lithium Plating Onset on Porous Graphite Electrodes Under Fast Charging with Hierarchical Multiphase Porous Electrode Theory. *J. Electrochem. Soc.* **2024**, *171* (1), No. 010526.
- (51) Williams, N. J.; et al. Electric Fields and Charge Separation for Solid Oxide Fuel Cell Electrodes. *Nano Lett.* **2022**, *22* (18), 7515–7521.
- (52) Quérel, E.; et al. Operando Characterization and Theoretical Modeling of Metall Electrolyte Interphase Growth Kinetics in Solid-State Batteries. Part I: Experiments. *Chem. Mater.* **2023**, *35* (3), 853–862.
- (53) Williams, N. J.; et al. Operando Characterization and Theoretical Modeling of Metall Electrolyte Interphase Growth Kinetics in Solid-State Batteries. Part II: Modeling. *Chem. Mater.* **2023**, *35* (3), 863–869.
- (54) Williams, N. J.; et al. Proton-Coupled Electron Transfer at SOFC Electrodes. *J. Chem. Phys.* **2023**, *158* (24), No. 244107.
- (55) Lees, E. W.; Bui, J. C.; Romiluyi, O.; Bell, A. T.; Weber, A. Z.; et al. Exploring CO₂ Reduction and Crossover in Membrane Electrode Assemblies. *Nat. Chem. Eng.* **2024**, 340–353.
- (56) Elgazzar, A.; Wang, H. Solvent Reorganization Model Takes the Lead. *Nat. Chem. Eng.* **2024**, 334–335.
- (57) Thaman, H.; Li, M.; Rose, J.; Narasimhan, S.; Xu, X.; Yeh, C.-N.; Jin, N.; Akbavsev, A.; Davidoff, I.; Bazant, M. Z.; Chueh, W. C. Two-Stage Growth of Solid Electrolyte Interphase on Copper: Imaging and Quantification by Operando Atomic Force Microscopy. *ACS nano* **2025**, *19* (12), 11949.

(58) Fraggedakis, D.; Bazant, M. Z. Tuning the Stability of Electrochemical Interfaces by Electron Transfer Reactions. *J. Chem. Phys.* **2020**, *152*, No. 184703.

(59) Kong, L.; Chen, J.-X.; Peng, H.-J.; Huang, J.-Q.; Zhu, W.; Jin, Q.; Li, B.-Q.; Zhang, X.; Zhang, Q. Current-Density Dependence of $\text{Li}_2\text{S}/\text{Li}_2\text{S}_2$ Growth in Lithium–Sulfur Batteries. *Energy Environ. Sci.* **2019**, *12*, 2976–2982.